Controlled Multi-source Mapping of Lunar South Polar Regions via Combined Bundle Adjustment

Qionghua You [1], Zhen Ye [1, 2] *, Yusheng Xu [1, 2], Rong Huang [1, 2], Huan Xie [1, 2], Xiaohua Tong [1, 2]

[1] College of Surveying and Geoinformatics, Tongji University, Shanghai, China
[2] The Shanghai Key Laboratory of Space Mapping and Remote Sensing for Planetary Exploration, Shanghai, China

Keywords: Lunar Orbiter Multi-source Data, Lunar South Pole, Permanently Shadowed Regions, Cross-modality Image Matching, Bundle Adjustment.

Abstract

Integration of LROC NAC and ShadowCam imagery is essential for meter-scale controlled mapping of the entire lunar south pole including Permanently Shadowed Regions (PSRs), but remains challenging due to extreme radiometric differences, sparse overlap across illumination boundaries, and ill-conditioned bundle adjustment networks. This paper proposes a LOLA DEM-mediated multi-source bundle adjustment framework for controlled lunar polar mapping. A hierarchical cross-modality matching strategy is developed using first- and second-order Gaussian steerable gradient features with multi-scale fusion and phase-correlation-based subpixel refinement. Sensor-specific geometric models are established using second-order polynomial transformations for NAC orthoimages and rational polynomial models for ShadowCam map-projected images. Five types of geometric constraints are formulated to integrate intra-sensor, limited cross-sensor, and image-to-DEM observations, with the LOLA DEM acting as a common geometric mediator. To stabilize the heterogeneous network, a hybrid L1-L2 regularization model with adaptive two-stage weighting is optimized using ADMM algorithm. Experiments in the lunar south polar region demonstrate substantial improvements on intra-sensor, cross-sensor, and image-to-reference positioning accuracy. The final seamless 1 m/pixel orthorectified mosaics achieve approximately 5 m absolute accuracy, validating the proposed framework for geometrically unifying illuminated and permanently shadowed terrain in lunar polar controlled mapping.

1. Introduction

High-resolution orthorectified mosaics of the lunar south polar region can reveal detailed surface morphology across both illuminated terrain and crater interiors (Collins et al., 2026; Robinson et al., 2012), playing an important role in future crewed landing missions and scientific exploration. They provide crucial support for selecting landing sites and identifying surface hazards (Daftry et al., 2023), and lay a solid foundation for characterizing Permanently Shadowed Regions (PSRs), which have not received direct sunlight for billions of years and represent high-priority science targets as potential repositories for water ice and volatile species (Grieser et al., 2024; Flahaut et al., 2020). Generally, the sensors available for south polar mapping can be categorized according to their radiometric capabilities: the Lunar Reconnaissance Orbiter Camera Narrow Angle Camera (LROC NAC, 0.5-2 *m/pixel*) for sunlit terrain (Robinson et al., 2010), and ShadowCam (~1.7 *m/pixel*, 200× sensitivity) for PSR imaging using secondary illumination from nearby crater walls and earthshine (Robinson et al., 2023). Mosaics based on single-sensor coverage have limited spatial completeness-NAC imagery yields no useful signal within PSR interiors, while ShadowCam cannot image sunlit terrain-which is insufficient to satisfy the demands of meter-scale controlled mapping bridging the illumination boundary for resource prospecting and traverse planning.

Recent advances in ShadowCam geometric processing have yielded notable progress. Wagner et al. (2024) demonstrated that over 95% of ShadowCam map-projected images achieve positioning accuracy within 60 meters under nominal ephemeris data, while Collins et al. (2024) produced 1 *m/pixel* multi-illumination controlled mosaics for Artemis III candidate sites by integrating LROC NAC and ShadowCam imagery. However, these workflows depend on proprietary sensor models and require extensive manual intervention for control point selection, limiting automation and scalability. Image-to-DEM registration based on structural gradient matching has achieved sub-pixel accuracy for NAC orthoimage co-registration (Xin et al., 2018; Liu et al., 2024b), but such approaches fail to extend to ShadowCam due to extreme radiometric disparity at illumination boundaries, where intensity distributions differ by orders of magnitude between secondary-illuminated imagery and DEM-derived shaded relief, defeating conventional feature descriptors.

Lunar photogrammetric block adjustment has been extensively developed for single-sensor configurations. Rigorous sensor models with LOLA altimetric control have been applied to Kaguya and LROC NAC imagery (Ostrach et al., 2023; Archinal et al., 2023; Henriksen et al., 2017), and joint adjustment incorporating LOLA laser points has improved planimetric and vertical accuracy (Haase et al., 2019; Wu et al., 2014). However, sparse co-visible areas along PSR boundaries-confined to narrow transitional zones-provide insufficient direct tie points for robust NAC-ShadowCam registration, and limited LOLA sampling density leaves local distortions inadequately constrained (Chen et al., 2024; Liu et al., 2024a). Without robust cross-sensor constraints, bundle adjustment of the combined network becomes ill-conditioned, causing sub-network fragmentation and systematic inter-sensor inconsistencies. A unified framework for meter-scale controlled mapping across the illumination boundary therefore remains an open problem.

* Corresponding author
E-mail addresses: 89_yezhen@tongji.edu.cn (Z. Ye).

Therefore, this study proposes a multi-source bundle adjustment framework, which transforms the cross-sensor registration problem into an indirect geometric mediation problem through the common DEM reference, and employs hybrid L1-L2 regularization to ensure solution stability under ill-conditioned network configurations. The framework integrates NAC orthoimages and ShadowCam map-projected imagery through a hierarchical cross-modality matching strategy and a five-type geometric constraint formulation. In this study, a small-scale validation experiment is conducted in the lunar south polar region to evaluate the proposed framework against the LOLA geodetic reference. The resulting seamless 1 *m/pixel* orthorectified mosaics achieve about 5 m absolute positional accuracy, representing the first controlled cartographic product that seamlessly bridges illuminated and permanently shadowed terrain at meter-scale resolution, satisfying geodetic requirements for polar exploration mission planning.

2. Method

The proposed controlled mapping framework consists of three components: hierarchical cross-modality image matching (Section 2.1), multi-source bundle adjustment mediated by LOLA DEM (Section 2.2), and Laplacian-based seamless mosaicking (Section 2.3). The overall workflow is illustrated in Figure 1.

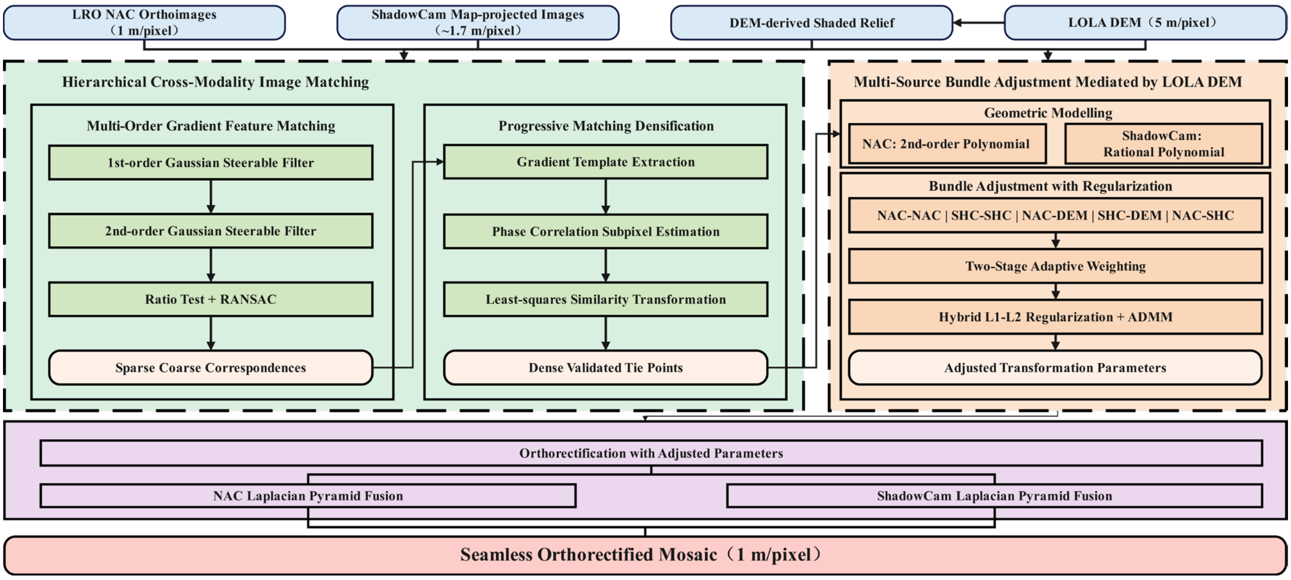

Figure 1. Overall workflow of the proposed multi-source bundle adjustment framework.

2.1 Hierarchical Cross-Modality Image Matching

Establishing geometric correspondences between optical imagery and DEM-derived products is challenging due to fundamentally disparate image formation mechanisms. Optical sensors capture surface reflectance governed by illumination geometry and albedo, whereas shaded relief is synthetically generated from topographic slope and aspect alone. Identical features thus yield entirely different intensity signatures across modalities, and conventional intensity-based matching algorithms fail. This gap is further exacerbated for ShadowCam imagery acquired under faint secondary illumination. To address this, a hierarchical cross-modality matching strategy operating in the structural gradient domain is developed. Despite intensity differences, gradient patterns remain geometrically consistent across modalities as they reflect the same underlying morphology. The strategy proceeds from sparse gradient-based feature matching to progressive densification through phase correlation refinement.

2.1.1 Multi-Order Gradient Feature Matching First-order gradients capture large-scale structural boundaries while second-order gradients provide finer edge and curvature detail. Integrating both orders yields modality-invariant representations that encode surface morphology independent of illumination conditions.

A first-order Gaussian steerable filter is employed to convolve the image across multiple directions for extracting contour information. The filter kernel and its convolution response at arbitrary orientation θ are defined as:

$$\begin{cases} G_{1,\sigma}^{\theta} = \cos(\theta)\dfrac{\partial G(I)}{\partial x} + \sin(\theta)\dfrac{\partial G(I)}{\partial y} \\ S_{1,\sigma}^{\theta} = G_{1,\sigma}^{\theta} * I(x,y) \end{cases} \tag{1}$$

where $G(I)$ is a 2D anisotropic Gaussian function, $\frac{\partial G(I)}{\partial x}$ and $\frac{\partial G(I)}{\partial y}$ are its first-order partial derivatives along x and y directions serving as the two basis filters at 0° and 90°, σ is the Gaussian standard deviation controlling scale, θ is the steering orientation angle, $I(x,y)$ is the input image, $S_{1,\sigma}^{\theta}$ is the directional edge response, and $*$ denotes 2D convolution. Six orientations are uniformly sampled over 0°–180° at 30° intervals. Multi-scale responses at three scales ($\sigma_k, k \in \{1,2,3\}$) are computed and adaptively fused:

$$E_k(x,y) = \max_{1 \le i \le N_\theta} \left| G_{1,\sigma_k}^{\theta_i} * I(x,y) \right| \tag{2}$$

$$F(x,y) = \sum_{k=1}^{3} \begin{cases} E_k(x,y), & if\ k = argmax_j \left| E_j(x,y) \right| \\ 0, & otherwise \end{cases} \tag{3}$$

https://doi.org/10.5194/isprs-archives-XLIX-B2-2026-93-2026 | © Author(s) 2026. CC BY 4.0 License.

where $E_k(x,y)$ is the maximum response across N_θ=6 orientations at scale k, and $F(x,y)$ is the fused multi-scale gradient map retaining only the dominant scale response at each pixel. Larger σ values suppress noise interference while smaller values preserve fine structural details.

Second-order Gaussian steerable filters are employed to capture curvature and fine edge structures complementary to first-order features (Wan et al., 2024). Analogous to the first-order case, the filter kernel is constructed from second-order partial derivatives of the 2D Gaussian function along *x*, *y*, and diagonal directions, serving as three basis filters. By weighted combination of these basis components, the second-order filter can be synthesized at arbitrary orientation θ to compute curvature responses that distinguish ridges, valleys, and saddle-point structures. The second-order filter is steered across the same six orientations (0°, 30°, 60°, 90°, 120°, 150°) as the first-order filter to maintain directional consistency.

KAZE (Alcantarilla et al., 2012) keypoints are detected in overlapping image blocks using combined first- and second-order gradient maps. Each keypoint neighborhood is transformed into log-polar coordinates with rotation normalization based on the dominant gradient direction. Gradient orientation histograms (8 bins) from both gradient orders are concatenated with the KAZE descriptor to form a 768-D composite vector. Matching uses Euclidean distance with ratio test, followed by Random Sample Consensus (RANSAC) to reject outliers and yield reliable coarse correspondences.

2.1.2 Progressive Matching Densification

Building upon the coarse correspondences, fine alignment refines feature point positions to subpixel accuracy. For each initial correspondence, a 121×121 pixel window is extracted from both reference and target images. Rather than using raw pixel intensities, template construction employs second-order steerable gradient responses, which effectively encode edge orientation and curvature information while suppressing radiometric discrepancies between modalities.

Phase correlation is adopted as the similarity measure for subpixel displacement estimation. By computing the normalized cross-power spectrum of the gradient-based templates in the Fourier domain, subpixel shifts are determined through precise localization of correlation peaks (Ye et al., 2018). This frequency-domain approach offers inherent robustness to local intensity variations and noise, making it particularly suitable for cross-modality matching scenarios. RANSAC-based outlier rejection is then applied to eliminate erroneous matches, and the final similarity transformation for each image block is computed via least-squares optimization.

2.2 Multi-Source Bundle Adjustment Mediated by LOLA DEM

Due to negligible direct overlap between NAC and ShadowCam imagery across the permanent shadow boundary, conventional bundle adjustment relying on inter-sensor tie points cannot establish geometric linkage between the two sensor networks. The LOLA DEM serves as a geometric mediator: both sensor types are independently matched to DEM-derived shaded relief products, and the resulting image-to-DEM correspondences implicitly define geometric relationships through their shared reference to absolute LOLA coordinates. This mediation strategy enables indirect cross-sensor registration while anchoring the entire network to a geodetically controlled reference frame.

2.2.1 Geometric Modelling

Sensor-specific transformation models are established to link image pixel coordinates and ground geographic coordinates for each data source, with model coefficients serving as the unknown parameters to be estimated in the bundle adjustment.

The LROC NAC imagery has undergone rigorous photogrammetric processing including bundle adjustment with LOLA altimetric control and orthorectification onto the LOLA DEM at 1 *m/pixel* ground sample distance. Despite this processing, minor residual planimetric errors persist due to accumulated uncertainties in spacecraft ephemeris, attitude determination, and DEM vertical accuracy. Given the spatially smooth and low-frequency characteristics of these residual distortions, a second-order polynomial transformation $f_{2\text{nd}}$ is adopted to parameterize the mapping from image pixel coordinates to ground geographic coordinates:

$$\begin{cases} (\mathrm{X},\mathrm{Y}) = f_{2\text{nd}}(a,b,r,c) \\ \mathrm{X} = a_0 + a_1 c + a_2 r + a_3 cr + a_4 c^2 + a_5 r^2 \\ \mathrm{Y} = b_0 + b_1 c + b_2 r + b_3 cr + b_4 c^2 + b_5 r^2 \end{cases} \tag{4}$$

where (r,c) denote image row and column coordinates, (X, Y) are the corresponding planimetric ground coordinates in the LOLA geodetic reference frame, and $a = \{a_0, \dots, a_5\}$, $b = \{b_0, \dots, b_5\}$ are twelve polynomial coefficients to be estimated. The affine components $(a_0 - a_2, b_0 - b_2)$ compensate for residual translation, rotation, and scale errors, while the quadratic terms $(a_3 - a_5, b_3 - b_5)$ account for higher-order systematic distortions arising from the aforementioned error sources.

The ShadowCam map-projected imagery is employed in this study. Although a rigorous sensor model based on collinearity equations would theoretically provide the most accurate geometric representation, precise Korea Pathfinder Lunar Orbiter (KPLO) platform ancillary data—particularly ephemeris and attitude determination records—are not readily available. This renders such an approach impractical for operational multi-source integration. To maintain geometric fidelity while circumventing this constraint, a generalized rational polynomial model f_{RPC} is adopted as a replacement sensor model to establish the mathematical mapping from ShadowCam projected image pixel coordinates to ground geographic coordinates as:

$$\begin{cases} (\mathrm{X},\mathrm{Y}) = f_{RPC}(c,d,r,c) \\ \mathrm{X} = P_1(r_n, c_n) / P_2(r_n, c_n) \\ \mathrm{Y} = P_3(r_n, c_n) / P_4(r_n, c_n) \end{cases} \tag{5}$$

where (X, Y) are ground planimetric coordinates, (r_n, c_n) are normalized image coordinates with $r_n = (r - r_0)/r_s$ and $c_n = (c - c_0)/c_s$, and $P_1 - P_4$ are third-order polynomials with up to 10 coefficients each. The rational polynomial formulation provides sufficient representational flexibility to approximate the complex geometric distortions in the projected products without requiring explicit sensor calibration parameters. Initial coefficients are estimated via least-squares fitting over a dense uniform grid imposed on each ShadowCam map-projected image, with the coefficients subsequently refined within the multi-source bundle adjustment.

2.2.2 Bundle Adjustment Model with Regularization

Multi-Source Geometric Constraint Formulation. The bundle adjustment simultaneously estimates the NAC polynomial coefficients (a,b) and ShadowCam rational polynomial coefficients (c,d) defined in Section 2.2.1 to enforce geometric consistency across the heterogeneous sensor network. Both transformation models f_{2nd} and f_{rpc} map from image pixel coordinates (r,c) to ground geographic coordinates (X,Y). Five constraint types are formulated as:

$$\begin{cases} v_{NAC-NAC} = f_{2\mathrm{nd}}(a_i,b_i,r_t,c_t) - f_{2\mathrm{nd}}(a_j,b_j,r_t',c_t') \\ v_{SHC-SHC} = f_{RPC}(c_i,d_i,r_t,c_t) - f_{RPC}(c_j,d_j,r_t',c_t') \\ v_{NAC-SHC} = f_{2\mathrm{nd}}(a_i,b_i,r_t,c_t) - f_{RPC}(c_i,d_i,r_t',c_t') \\ v_{NAC-DEM} = f_{2\mathrm{nd}}(a_i,b_i,r_m,c_m) - (\mathrm{X}_{DEM},\mathrm{Y}_{DEM}) \\ v_{SHC-DEM} = f_{RPC}(c_i,d_i,r_m,c_m) - (\mathrm{X}_{DEM},\mathrm{Y}_{DEM}) \end{cases} \tag{6}$$

where (r_t, c_t) and (r_t', c_t') are pixel coordinates of the same tie point in images i and j, (r_m, c_m) are pixel coordinates of DEM control points, (X_{DEM}, Y_{DEM}) are known LOLA DEM geographic coordinates, and residuals v quantify planimetric discrepancies. Intra-sensor constraints (NAC-NAC, SHC-SHC) enforce that overlapping images from the same sensor yield consistent geographic coordinates for shared tie points. Cross-sensor constraints (NAC-SHC), available only in limited transitional zones, provide direct inter-network linkage. Image-to-DEM constraints (NAC-DEM, SHC-DEM) anchor both sensors to the absolute LOLA reference. Due to negligible direct overlap across the shadow boundary, the LOLA DEM serves as geometric mediator for indirect cross-sensor registration. Linearizing via first-order Taylor expansion yields:

$$v = A\Delta x - b \tag{7}$$

where Δx contains corrections to all NAC and ShadowCam model coefficients, A is the sparse Jacobian matrix, and b is the misclosure vector. The weighted normal equations are:

$$NDx = c,\ N = A^T WA,\ \mathrm{c} = A^T Wb \tag{8}$$

Regularized Optimization Image-to-DEM correspondences from cross-modality matching exhibit lower reliability than image-to-image ties, with heavier-tailed error distributions and higher gross error proportions. Their sparse and heterogeneous spatial distribution causes ill-conditioning of the normal equation matrix.

A two-stage weighting strategy addresses this heterogeneity. Stage 1 assigns reduced weights to DEM constraints to establish geometric linkage while limiting gross error propagation. After initial convergence, observations with standardized residuals exceeding $3\hat{\sigma}_0$ are removed. Stage 2 increases DEM weights to anchor both sensor networks to the absolute LOLA reference.

Residual ill-conditioning persists in weakly constrained network portions. Standard L2 regularization lacks outlier robustness, while L1 regularization may introduce artificial discontinuities. A hybrid L1-L2 scheme simultaneously stabilizes the normal equations and suppresses residual outliers:

$$\min_{\Delta x} \left\| W^{1/2}(A x - b) \right\|_2^2 + \theta \left\| D\Delta x \right\|_1 + \delta \left\| D\Delta x \right\|_2^2 \tag{9}$$

where D is a first-order differencing matrix with $(D\Delta x)_{ij} = \Delta x_i - \Delta x_j$ for adjacent images. The L1 term (coefficient θ) suppresses abrupt parameter variations from residual gross errors while preserving genuine discontinuities. The L2 term (coefficient δ) ensures parameter continuity in weakly constrained regions (Han et al., 2025).

ADMM Optimization The non-differentiability of the L1 norm in the composite objective function precludes direct solution via standard least-squares or gradient-based methods. The Alternating Direction Method of Multipliers (ADMM) is employed to decompose the non-smooth optimization into a sequence of tractable subproblems through variable splitting (Parikh et al., 2011). By introducing an auxiliary variable $z = D\Delta x$ and a scaled dual variable u, the augmented Lagrangian formulation decouples the L1 and L2 regularization terms, enabling each to be handled by its respective closed-form solver. The iterative scheme alternates between three updates: a parameter update step solved via sparse Cholesky factorization, a soft-thresholding step that enforces L1 sparsity on the auxiliary variable, and a dual variable update that enforces the coupling constraint between parameters and auxiliary variables. The regularization coefficients θ and δ are adaptively tuned throughout the iteration based on the ratio of primal and dual residual norms, ensuring balanced convergence without manual parameter selection. Upon convergence, a bias correction procedure is applied to remove residual low-frequency systematic trends.

2.3 Image Stitching Based on Two-Level Laplacian Fusion

Following geometric adjustment, the corrected orthoimages within each sensor network are seamlessly blended to produce the final mosaic. Radiometric heterogeneity among same-source images presents significant challenges: NAC orthoimages exhibit substantial intensity variations due to differing solar illumination geometries across acquisition epochs, while overlapping ShadowCam images display radiometric gradients arising from spatially varying secondary illumination conditions within PSRs. Direct averaging or simple feathering produces visible seams at image boundaries where these intra-sensor radiometric discontinuities occur.

A two-level Laplacian pyramid fusion strategy is adopted independently for NAC orthoimage mosaicking and ShadowCam image mosaicking (Li et al., 2020). Each orthoimage is decomposed into low-frequency and high-frequency components through Gaussian filtering-the former capturing the smooth background illumination field and large-scale radiometric gradients, the latter encoding fine-scale textural detail, edge information, and surface morphological features. Blending weights for each pixel are computed via distance transforms measuring proximity to image boundaries, with pixels near image centers receiving higher weights to create smooth transition zones in overlapping regions.

The blending proceeds independently at each pyramid level: low-frequency components are blended using distance-weighted masks to achieve smooth radiometric transitions across image boundaries, while high-frequency components are blended to preserve fine textural detail. The final mosaic is reconstructed by summing the blended components, producing seamless products that maintain radiometric continuity while preserving surface detail.

3. Experimental results and discussions

Dataset and Pre-Processing A validation experiment was conducted in the lunar south polar region, characterized by extreme illumination contrasts between sunlit terrain and permanently shadowed crater interiors. The dataset comprises 224 LROC NAC images and 48 ShadowCam images covering 26 PSRs (>1 km^2), selected based on coverage and overlap criteria (Ye et al., 2025), with a 5 *m/pixel* LOLA DEM as geodetic reference (Barker et al., 2023). NAC images were processed through USGS ISIS (Sides et al., 2017), including radiometric calibration, echo correction, and SPICE kernel integration, then bundle-adjusted with LOLA altimetry and orthorectified to 1 *m/pixel*. ShadowCam PSR boundaries were delineated via connected-component analysis with manual refinement. All imagery was reprojected to the Moon2000 South Polar Stereographic projection at 1 *m/pixel*.

Positioning Accuracy Quantitative validation evaluated RMSE for relative and absolute positioning accuracy under three conditions: pre-adjustment, conventional bundle adjustment (without regularization), and the proposed method.

Table 1 presents relative accuracy stratified by constraint type. The ShadowCam-related constraints dominate the overall error budget: SHC-SHC pre-adjustment residuals reach 12.917 m (X) and 7.282 m (Y), an order of magnitude larger than NAC-NAC (0.215 m, 0.186 m), reflecting substantial systematic planimetric inconsistencies in ShadowCam map-projected products due to limited KPLO ephemeris precision. Conventional adjustment reduces SHC-SHC to 5.834 m and 3.127 m, while the proposed method further decreases these to 2.516 m and 1.654 m, achieving 80.5% and 77.3% overall improvements. This additional reduction over conventional adjustment demonstrates that hybrid L1-L2 regularization effectively suppresses outlier-contaminated correspondences that propagate into parameter estimates under standard least-squares weighting. LOLA-SHC constraints retain the largest post-adjustment residuals (4.328 m and 3.389 m), reduced from pre-adjustment values of 13.762 m and 8.274 m, attributable to the inherent modality gap between ShadowCam imagery and DEM-derived shaded relief. In contrast, NAC-related constraints converge to sub-meter levels: NAC-NAC reaches 0.104 m and 0.118 m, and LOLA-NAC achieves 0.819 m and 0.795 m, reflecting the higher geometric maturity of pre-processed NAC orthoimages and stronger image-to-DEM matching quality under direct solar illumination.

Table 2 aggregates the constraint-level results into three accuracy categories for network-level assessment. Intra-sensor accuracy, dominated by the ShadowCam component, improves from 5.296 m and 3.025 m pre-adjustment to 2.435 m and 1.345 m with conventional adjustment, and further to 1.069 m and 0.733 m with the proposed method, confirming that both sub-networks achieve substantially tighter internal consistency. Cross-sensor accuracy reaches 3.847 m (X) and 2.165 m (Y), reduced from 14.124 m and 8.356 m pre-adjustment, demonstrating that the DEM-mediated constraint architecture provides sufficient geometric coupling to prevent NAC-ShadowCam sub-network fragmentation and enforce continuity across the illumination boundary. Image-to-reference accuracy of 2.047 m and 1.703 m, improved from 6.903 m and 4.127 m, satisfies the geodetic requirements for meter-scale controlled mapping, indicating effective anchoring to the LOLA reference without the typical trade-off where tightening absolute control degrades internal coherence.

Constraint Type	Pre-adjustment (m)		Conventional BA (m)		Proposed Method (m)	
	X	Y	X	Y	X	Y
SHC-SHC	12.917	7.282	5.834	3.127	2.516	1.654
NAC-SHC	14.124	8.356	8.873	7.012	3.847	2.165
LOLA-SHC	13.762	8.274	9.215	7.103	4.328	3.389
NAC-NAC	0.215	0.186	0.168	0.157	0.104	0.118
LOLA-NAC	3.210	1.894	1.726	1.243	0.819	0.795

Table 1. Relative positioning accuracy by constraint type before and after adjustment.

Accuracy Type	Pre-adjustment (m)		Conventional BA (m)		Proposed Method (m)	
	X	Y	X	Y	X	Y
Intra-sensor	5.296	3.025	2.435	1.345	1.069	0.733
Cross-sensor	14.124	8.356	8.873	7.012	3.847	2.165
Image-to-reference	6.903	4.127	4.347	3.294	2.047	1.703

Table 2. Overall positioning accuracy comparison among three adjustment strategies.

To visually demonstrate the adjustment performance, three key regions-de Gerlache, Slater, and Nobile craters-are selected as representative areas, which are high-priority candidate sites for lunar polar exploration.

The geometric consistency improvement is visually confirmed in Figures 2 and 3. In Figure 2, the red lines indicate the original positional offsets between overlapping NAC and ShadowCam images. Before adjustment, systematic offsets of 5-15 m manifest as feature misalignment between the two sensor types. After adjustment, offsets are reduced to approximately 2-5 m levels with coherent spatial registration. Figure 3 presents the intra-sensor geometric consistency for ShadowCam imagery, where the red lines similarly denote the original positional deviations among overlapping ShadowCam images. The post-adjustment results demonstrate significantly improved internal consistency within the ShadowCam network.

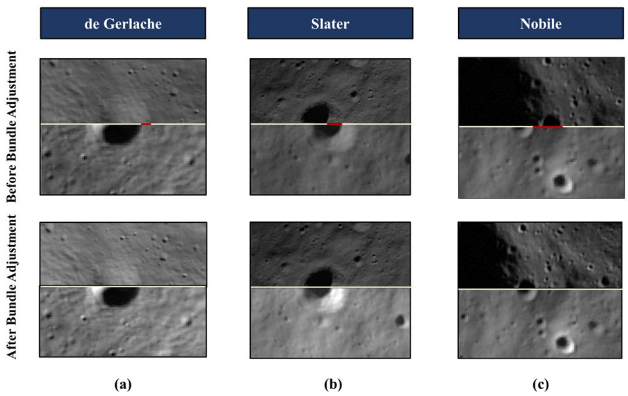

Figure 2. Cross-sensor geometric consistency comparison of three key regions (de Gerlache, Slater, and Nobile craters) before (top) and after (bottom) bundle adjustment, with overlaid LROC NAC and ShadowCam imagery. Red lines indicate original positional offsets.

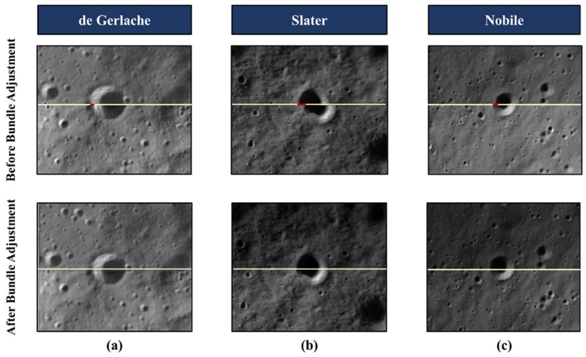

Figure 3. Intra-sensor geometric consistency comparison of ShadowCam imagery in three key regions (de Gerlache, Slater, and Nobile craters) before (top) and after (bottom) bundle adjustment. Red lines indicate original positional deviations.

Mosaicking Quality The same three representative regions-de Gerlache, Slater, and Nobile craters-are selected to evaluate mosaicking performance (Figure 4): de Gerlache at the NAC-ShadowCam transition boundary, Slater with entirely ShadowCam coverage under varying secondary illumination, and Nobile with multiple overlapping images under different illumination conditions.

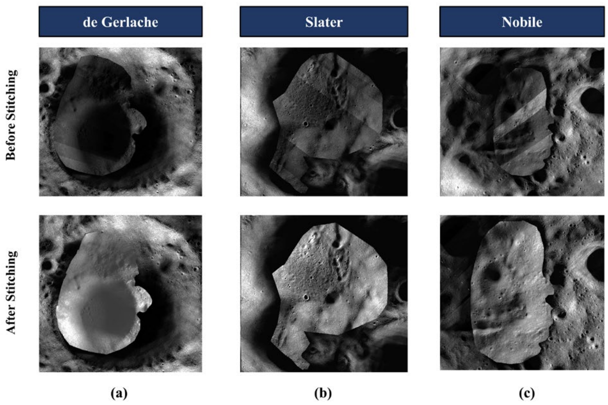

Figure 4. Mosaicking comparison of three key regions (de Gerlache, Slater, and Nobile craters) before (top) and after (bottom) seamless stitching.

The product enables reliable spatial correlation with complementary polar datasets and supports continuous traverse analysis from sunlit operational areas into PSR science targets without geometric discontinuities at the shadow boundary.

4. Conclusion

In this paper, we proposed a LOLA DEM-mediated multi-source bundle adjustment framework for controlled mapping of the lunar south polar region. The framework employs hierarchical cross-modality matching to establish reliable correspondences across the radiometric disparity between NAC and ShadowCam imagery, a five-type geometric constraint formulation with LOLA DEM as geometric mediator to overcome sparse inter-sensor overlap, and hybrid L1-L2 regularization via ADMM to stabilize the ill-conditioned network geometry. With the proposed framework, geometrically consistent co-utilization of the two heterogeneous sensor datasets is achieved, anchoring both networks to the LOLA geodetic reference. A validation experiment conducted in the lunar south polar region with 224 NAC and 48 ShadowCam images demonstrates that the framework produces seamless 1 *m/pixel* orthorectified mosaics satisfying approximately 5 m absolute accuracy requirements, constituting the first controlled cartographic product that geometrically unifies illuminated and permanently shadowed polar terrain at meter-scale resolution. In the future, we will extend the framework to broader coverage, addressing challenges in scalable optimization for increased image volumes, more complex network topology, and greater topographic relief variation.

Acknowledgment

This work was supported in part by the National Natural Science Foundation of China under Grant 42571517, in part by the Shanghai Municipal Natural Science Foundation under Grant 25ZR1401364, and in part by the Fundamental Research Funds for the Central Universities.

REFERENCES

Alcantarilla, P.F., Bartoli, A., Davison, A.J., 2012. KAZE features. *European Conference on Computer Vision*, Springer, 214-227.

Archinal, B.A., Weller, L.A., Richie, J.O., Lee, E.M., Bennett, K.A., Speyerer, E.J., Tyburczy, T., 2023. Controlled high-resolution LROC NAC Polar mosaics. *54th Lunar and Planetary Science Conference*, 2806, 2333.

Barker, M.K., Mazarico, E., Neumann, G.A., Smith, D.E., Zuber, M.T., Head, J.W., Sun, X., 2023. A new view of the lunar south pole from the lunar orbiter laser altimeter (LOLA). *The Planetary Science Journal*, 4(9), 183.

Chen, C., Ye, Z., Xu, Y., Liu, D., Huang, R., Zhou, M., Xie, H., Tong, X., 2024. Large-scale block bundle adjustment of LROC NAC images for lunar south pole mapping based on topographic constraint. *IEEE Journal of Selected Topics in Applied Earth Observations and Remote Sensing*, 17, 2731-2746.

Collins, W.M., Brown, H.M., Henriksen, M.R., Wagner, R.V., Boyd, A.K., Robinson, M.S., Chou, W.P., Carr, N.F., Grieser, S.A., Burnette, S.R., et al., 2024. Optimized Illuminated Terrain Coverage of the Candidate Artemis III Landing Sites with LROC NAC and ShadowCam Controlled Mosaics. *55th Lunar and Planetary Science Conference*, 3040, 1775.

Collins, W.M., Grieser, S.A., Henriksen, M.R., Clark, J.D., Carr, N.F., Wagner, R.V., Roseborough, T.A., Nystrom, S.E., Robinson, M.S., 2026. Photogrammetric processing of regional ShadowCam and LROC NAC controlled mosaics, evaluation of positional accuracies, and scientific applications. *Remote Sensing*, 18(3), 525.

Daftry, S., Chen, Z., Cheng, Y., Tepsuporn, S., Khattak, S., Matthies, L., Coltin, B., Naal, U., Ma, L.M., Deans, M., 2023. LunarNav: Crater-based localization for long-range autonomous lunar rover navigation. *2023 IEEE Aerospace Conference*, 1-15.

Flahaut, J., Carpenter, J., Williams, J.-P., Anand, M., Crawford, I.A., Van Westrenen, W., Füri, E., Xiao, L., Zhao, S., 2020. Regions of interest (ROI) for future exploration missions to the lunar South Pole. *Planetary and Space Science*, 180, 104750.

Grieser, S., Henriksen, M., Wagner, R., Mahanti, P., Manheim, M., Robinson, M., 2024. Investigation of Lunar Polar Regions using ShadowCam Mosaics. *45th COSPAR Scientific Assembly*. Held 13-21 July, 45, 295.

Haase, I., Gläser, P., Oberst, J., 2019. Bundle adjustment of spaceborne double-camera push-broom imagers and its application to LROC NAC imagery. The International Archives of the Photogrammetry, *Remote Sensing and Spatial Information Sciences*, 42, 1397-1404.

Han, J., Zhang, Z., Zheng, S., Fu, Q., Song, W., Ding, H., Wang, M., Huang, W., 2025. Novel Regularization Method of Adaptively Balanced L1 and L2 Norms with Bias Removal. *Journal of Surveying Engineering*, 151(4), 04025011.

Henriksen, M.R., Manheim, M.R., Burns, K.N., Seymour, P., Speyerer, E.J., Deran, A., Boyd, A.K., Howington-Kraus, E., Rosiek, M.R., Archinal, B.A., et al., 2017. Extracting accurate and precise topography from LROC narrow angle camera stereo observations. *Icarus*, 283, 122-137.

Li, H., Wang, J., Han, C., 2020. Image mosaic and hybrid fusion algorithm based on pyramid decomposition. *2020 International Conference on Virtual Reality and Visualization (ICVRV)*, 205-208.

Liu, P., Geng, X., Li, T., Zhang, J., Wang, Y.Y., Peng, Z., Wang, Y.H., Ma, X., Wang, Q., 2024a. The generation of high-resolution mapping products for the lunar south pole using photogrammetry and photoclinometry. *Remote Sensing*, 16(12), 2097.

Liu, P., Geng, X., Wang, Y., Zhang, J., 2024b. LOLA DEM assisted photogrammetric processing of lunar reconnaissance orbiter NAC images for the lunar south pole. The International Archives of the Photogrammetry, *Remote Sensing and Spatial Information Sciences*, 48, 409-416.

Ostrach, L.R., Weller, L.A., Wheeler, B.H., 2023. Creation of a near-global lunar control network using Kaguya terrain camera data, progress report. *54th Lunar and Planetary Science Conference*, 2806, 2735.

Parikh, N., Chu, E., Peleato, B., Eckstein, J., 2011. Distributed optimization and statistical learning via the alternating direction method of multipliers. *Foundations and Trends in Machine Learning*, 3(1), 1-122.

Robinson, M.S., Brylow, S.M., Tschimmel, M., Humm, D., Lawrence, S.J., Thomas, P.C., Denevi, B.W., Bowman-Cisneros, E., Zerr, J., Ravine, M.A., et al., 2010. Lunar reconnaissance orbiter camera (LROC) instrument overview. *Space Science Reviews*, 150(1), 81-124.

Robinson, M.S., Speyerer, E.J., Boyd, A., Waller, D., Wagner, R.V., Burns, K.N., 2012. Exploring the Moon with the lunar reconnaissance orbiter camera. The International Archives of the Photogrammetry, *Remote Sensing and Spatial Information Sciences*, 39, 501-504.

Robinson, M.S., Brylow, S.M., Caplinger, M.A., Carter, L.M., Clark, M.J., Denevi, B.W., Estes, N.M., Humm, D.C., Mahanti, P., Peckham, D.A., et al., 2023. ShadowCam instrument and investigation overview. *Journal of Astronomy and Space Sciences*, 40(4), 149-171.

Sides, S.C., Becker, T.L., Becker, K.J., Edmundson, K.L., Backer, J.W., Wilson, T.J., et al., 2017. The USGS Integrated Software for Imagers and Spectrometers (ISIS 3) instrument support, new capabilities, and releases. *48th Lunar and Planetary Science Conference*, 2739.

Wagner, R.V., Speyerer, E.J., Robinson, M.S., 2024. Cartographic Accuracy of ShadowCam Images. *55th Lunar and Planetary Science Conference*, 3040, 2357.

Wan, G., Ye, Z., Xu, Y., Huang, R., Zhou, Y., Xie, H., Tong, X., 2024. Multimodal remote sensing image matching based on weighted structure saliency feature. *IEEE Transactions on Geoscience and Remote Sensing*, 62, 1-16.

Wu, B., Hu, H., Guo, J., 2014. Integration of Chang'E-2 imagery and LRO laser altimeter data with a combined block adjustment for precision lunar topographic modeling. *Earth and Planetary Science Letters*, 391, 1-15.

Xin, X., Liu, B., Di, K., Jia, M., Oberst, J., 2018. High-precision co-registration of orbiter imagery and digital elevation model constrained by both geometric and photometric information. *ISPRS Journal of Photogrammetry and Remote Sensing*, 144, 28-37.

Ye, Z., Liu, D., Xu, Y., Huang, R., Zhou, M., Xiao, C., Xie, H., Tong, X., 2025. Optimal Selection of Stereo Image Pairs in Planetary Mapping Based on Local and Global Constraints. *IEEE Transactions on Geoscience and Remote Sensing.* 63, 1-17.

Ye, Z., Tong, X., Zheng, S., Guo, C., Gao, S., Liu, S., Xu, X., Jin, Y., Xie, H., Liu, S., et al., 2018. Illumination-robust subpixel Fourier-based image correlation methods based on phase congruency. *IEEE Transactions on Geoscience and Remote Sensing*, 57(4), 1995-2008.

https://doi.org/10.5194/isprs-archives-XLIX-B2-2026-93-2026